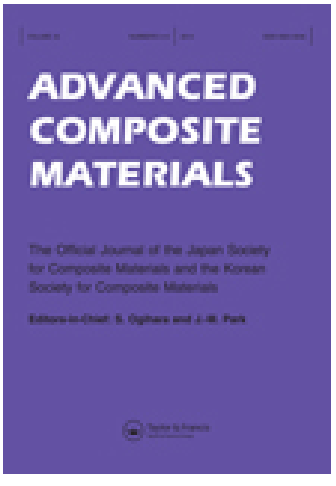

Advanced Composite Materials
Publication details, including instructions for authors and subscription information:
http://www.tandfonline.com/loi/tacm20

Multiscale approach to predict crack initiation in unidirectional off-axis laminates

Y. Sato[a], T. Okabe[a], R. Higuchi[a] & K. Yoshioka[b]

[a] Department of Aerospace Engineering, Tohoku University, 6-6-01 Aoba-yama, Aoba-ku, Sendai Miyagi, 980-8579, Japan

[b] Toray Composites (America), Inc., 19002 50th Avenue East, Tacoma, WA 98446, USA

Published online: 20 May 2014.

To cite this article: Y. Sato, T. Okabe, R. Higuchi & K. Yoshioka (2014) Multiscale approach to predict crack initiation in unidirectional off-axis laminates, Advanced Composite Materials, 23:5-6, 461-475, DOI: 10.1080/09243046.2014.915100

To link to this article: http://dx.doi.org/10.1080/09243046.2014.915100

Advanced Composite Materials, 2014
Vol. 23, Nos. 5–6, 461–475, http://dx.doi.org/10.1080/09243046.2014.915100

Multiscale approach to predict crack initiation in unidirectional off-axis laminates

Y. Sato[a], T. Okabe[a]*, R. Higuchi[a] and K. Yoshioka[b]

[a]*Department of Aerospace Engineering, Tohoku University, 6-6-01 Aoba-yama, Aoba-ku, Sendai Miyagi, 980-8579, Japan;* [b]*Toray Composites (America), Inc., 19002 50th Avenue East, Tacoma, WA 98446, USA*

(*Received 31 January 2013; accepted 5 March 2014*)

Crack initiation in unidirectional off-axis laminates made of carbon fiber and epoxy resin is predicted based on multiscale modeling. This multiscale modeling consists of two finite-element analyses (FEA) on different scales. One is macroscopic FEA, based on the assumption of homogeneous materials, and the other is microscopic periodic unit-cell (PUC) analysis using a micromechanical model. The macroscopic FEA is performed by applying uniaxial tension to off-axis laminates, in which we employ an anisotropic elasto-plastic constitutive law to obtain accurate deformation fields in laminates. In the microscopic PUC analysis, the strain history at a point in laminates obtained from the macroscopic FEA is applied as external forces, and crack initiation is predicted using two failure criteria for the matrix resin. The first is the dilatational energy density criterion under elastic deformation, and the second is a ductile damage growth law under plastic deformation. The simulated predictions are compared with the experiments results.

Keywords: composite materials; crack initiation; multiscale modeling; dilatational energy density; ductile damage growth

1. Introduction

Carbon-fiber-reinforced plastics (CFRP) offer the benefits of higher specific strength and stiffness than do conventional metal materials. Therefore, engineering applications of CFRP have been spreading rapidly for aerospace structures to reduce weight and fuel consumption. Laminates of angled unidirectional CFRP are often used in these applications, and complex combined stress/strain states appear in general laminates. The prediction of failure in laminates under these complex stress/strain states is important for engineering applications, so many researchers have studied the failure problem.

A major aspect of the failure problem has been the propagation problem. We often see in the literature a progressive failure analysis using cohesive zone modeling (CZM) [1,2] for delamination. These studies have succeeded in reproducing the fracture patterns and the final strength of general laminates. However, predicting crack initiation in laminates is difficult even now. Initial damage in composites, such as cracking in the matrix or interfacial debonding between fiber and matrix, occurs in microscopic structures. A conventional homogenized finite-element analysis (FEA), which does not distinguish between fiber and matrix resin, intrinsically has difficulty predicting crack initiation

*Corresponding author. Email: okabe@plum.mech.tohoku.ac.jp

since the deformation fields in internal microscopic structures cannot be simulated. Therefore, multiscale approaches are required to predict crack initiation in composites.

During the last decade, multiscale modeling has been developed to predict the initial damage occurring in composite materials.[3,4] Canal et al. [3] performed two-dimensional periodic unit-cell (PUC) analyses using the Jeong model [5] based on the Gurson model [6] for matrix resin. CZM was also used for interfacial debonding between fiber and matrix resin. They applied certain combined loading conditions under transverse tension and out-of-plane shear, and compared the simulated results with traditional failure criteria. We applied the Gurson–Tvergaard–Needleman (GTN) [6–9] model for matrix resin in our PUC model, and investigated the effect of fiber arrangement on crack initiation under transverse tension.[4] We also employed a realistic microstructure model in which fibers were located in a realistic arrangement, and confirmed that the simulated cracking position was consistent with the experiments.[10] These studies employed a ductile damage growth law under plastic deformation for the matrix resin. On the other hand, Asp et al. [11,12] claimed that the stress state in the matrix near the pole of a fiber becomes triaxial due to constraints imposed by the stiff fiber, resulting in the cavitation-induced brittle failure that occurs under elastic deformation. They successfully predicted the failure strain under transverse tension using the dilatational energy density criterion for the matrix. These studies indicate that crack initiation can be predicted by multiscale approaches, although the modeling of damage mechanisms differs in each case. However, the analyses mentioned above were performed under uniaxial transverse tension or virtual simple combined loadings. Therefore, we need to discuss the validity of these multiscale analyses in more practical problems such as general angled laminates.

For this study, we applied a multiscale approach to predict crack initiation in composites deformed under general conditions. We simulated crack initiation in unidirectional off-axis laminates with combined stress states of tension and in-plane shear. This multiscale modeling consisted of two FEA models on different scales. The first is macroscopic FEA, assuming composites to be homogeneous materials, and the second is microscopic FEA, using a three-dimensional (3D) PUC model consisting of fibers and matrix resin. In the microscopic analysis, we employed two failure criteria under elastic and plastic deformation. In addition, we performed a series of uniaxial tensile tests for off-axis laminates with different angles, and compared the results with simulated predictions.

2. Multiscale modeling

2.1. *Macroscopic FEA*

Macroscopic 3D FEA of unidirectional off-axis laminates is performed by applying uniaxial tensile loading. Off-axis specimens exhibit nonlinear behavior when loaded because of plastic deformation in the matrix resin. Therefore, we need to model the macroscopic nonlinear behavior to accurately predict deformation fields in specimens. We apply an anisotropic elasto-plastic constitutive law that was modified by Yokozeki et al. [13] based on the elasto-plastic law proposed by Sun and Chen [14]. In this constitutive model, the effective stress $\bar{\sigma}$ and yield function f are defined by the stress components in coordinate system of the material principal directions as follows.

$$\bar{\sigma} = \sqrt{\frac{3}{2}\left\{(\sigma_{22}-\sigma_{33})^2 + 2a_{44}\sigma_{23}^2 + 2a_{66}(\sigma_{12}^2+\sigma_{13}^2)\right\} + a_1^2\sigma_{11}^2} + a_1(\sigma_{11}+\sigma_{22}+\sigma_{33}), \tag{1}$$

$$\bar{\sigma} = \sqrt{3f}. \tag{2}$$

Here, 1, 2, and 3 are the material principal directions: 1 is the fiber axial direction, 2 is the in-plane transverse direction, and 3 is the out-of-plane transverse direction. a_{44}, a_{66}, and a_1 are constants controlling the plastic behavior. We referred to the literature and employed $a_{44} = 2.0$ and $a_1 = 0.01$.[13,15] $a_{66} = 1.6$ is determined from the experiment results mentioned in Section 3. This constitutive law includes the hydrostatic dependence of plasticity, enabling us to reproduce the difference between the tensile and compressive yielding. The detail of the plasticity model is described in the literature, [13] in which we can see an explicit form of the stress–strain relationship for a plane-stress condition.

The master relationship of the effective stress $\bar{\sigma}$ and effective strain $\bar{\varepsilon}^p$ for plastic behavior is approximated by the following power laws.

$$\bar{\varepsilon}^p = A_1(\bar{\sigma})^{n_1} \text{ for } \bar{\sigma} < \bar{\sigma}_{threshold} \tag{3}$$

$$\bar{\varepsilon}^p = A_2(\bar{\sigma})^{n_2} \text{ for } \bar{\sigma} \geq \bar{\sigma}_{threshold} \tag{4}$$

Here, we use two sets of fitting constants, A_1, n_1, and A_2, n_2, to reproduce the nonlinear behavior precisely, in the same way as in [15]. These constants are determined so that the power laws reproduce the master curve obtained by the experiments described in Section 3. The constants used in this plasticity model are summarized in Table 1.

The angles of fiber direction in the unidirectional laminates were 15°, 20°, 30°, 45°, 60°, 75°, and 90°. The macroscopic FEA is then analyzed using an incremental algorithm. The finite-element model of laminates is modeled by eight-node brick elements (Figure 1). We use a FE model with 10-times length of actual specimens. The

Table 1. Constants used in the anisotropic plasticity model for unidirectional off-axis CFRP laminates in macroscopic 3D FEA.

a_{44}	a_{66}	a_1	A_1	n_1	A_2	n_2	$\bar{\sigma}_{threshold}$
2.0	1.6	0.01	3.2×10^{-11}	3.8	4.5×10^{-18}	7.0	138 MPa

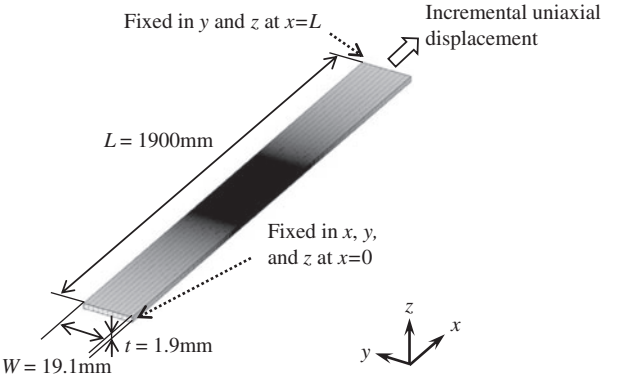

Figure 1. 3D FE model for macroscopic analysis.

reason for employing the model is described later. The elastic properties of unidirectional CFRP used in these simulations are listed in Table 2.

2.2. Microscopic PUC analysis

To predict the initiation of cracks in off-axis laminates, we employ 3D PUC modeling consisting of fibers and matrix (Figure 2). In this study, we only focus on damage in the matrix, with the interface between fiber and matrix assumed to be perfectly bonding. The fiber is treated as an orthotropic elastic, and the matrix resin is assumed to be an isotropic elasto-viscoplastic body. Both components are modeled by 10-node tetrahedral elements. Applying a periodic boundary condition to the model enables us to eliminate the virtual edge problem in the model. The unit cell includes five fibers (Figure 2). The fiber diameter is 7 μm, and the length of each side of the unit cell is determined by making the fiber volume fraction 56%.

The elasto-viscoplastic constitutive relationship of the matrix element, including damage parameter D, is presented as follows,[16] based on the hypothesis of strain equivalence.[17–19]

$$\dot{\boldsymbol{\sigma}} = (1-D)\boldsymbol{C}_m^e : \dot{\boldsymbol{\varepsilon}} - (1-D)\frac{3\mu\dot{\bar{\varepsilon}}^p}{\bar{\sigma}}\boldsymbol{\sigma}' - \frac{\dot{D}}{1-D}\boldsymbol{\sigma} \tag{5}$$

Table 2. Elastic properties of unidirectional CFRP laminates used in macroscopic 3D FEA.

Longitudinal Young's modulus E_1	130 GPa
Transverse Young's modulus E_2, E_3	8.21 GPa
Shear modulus G_{12}, G_{13}	4.00 GPa
Shear modulus G_{23}	2.77 GPa
Poisson's ratio v_{12}, v_{13}	0.26
Poisson's ratio v_{23}	0.48

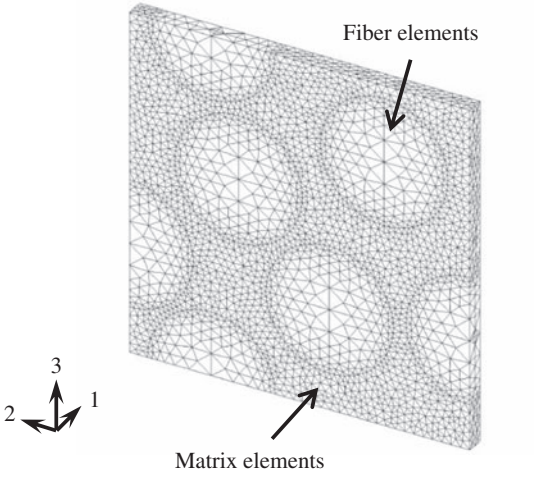

Figure 2. 3D FE model for microscopic PUC analysis.

Here, $\boldsymbol{\sigma}$ is the stress tensor, $\boldsymbol{C}_m^e$ is the elastic stiffness tensor, $\boldsymbol{\varepsilon}$ is the strain tensor, μ is the shear modulus, $\bar{\sigma}$ is the von Mises stress, and $\boldsymbol{\sigma}'$ is the deviatoric stress tensor. Superscript $\cdot$ indicates time-differentiation. The equivalent plastic strain rate $\dot{\bar{\varepsilon}}^p$ is determined by the following equation, presented by Matsuda et al. [20], which is a hardening rule involving the effect of hydrostatic stress on an epoxy resin.

$$\dot{\bar{\varepsilon}}^p = \dot{\varepsilon}_r \left(\frac{\bar{\sigma} + \beta \sigma_m}{g(\bar{\varepsilon}^p)} \right)^{\frac{1}{m}} \tag{6}$$

$$\text{where } g(\bar{\varepsilon}^p) = g_1 (\bar{\varepsilon}^p)^{g_2} + g_3 \tag{7}$$

Here, m is an exponent regarding strain-rate sensitivity, $\dot{\varepsilon}_r$ is a reference strain rate, σ_m is the hydrostatic stress, and β is hydrostatic stress sensitivity. This study assumes $m = 1/35$, $\dot{\varepsilon}_r = 1 \times 10^{-5}$, and $\beta = 0.2$. Here, g_1, g_2, and g_3 are material constants determined as: $g_1 = 90$, $g_2 = 0.08$, and $g_3 = 20$ MPa. The linearity limit of the epoxy resin $\bar{\sigma}_Y$ was 75 MPa in this study. The material constants regarding the elastic properties of fiber and matrix are listed in Table 3.

This study employs two failure criteria for matrix resin. The first is the dilatational energy density criterion reported by Asp et al. [11,12]. This failure criterion is valid under triaxial and elastic deformation which appears in matrix resin near the poles of the fibers in composites under transverse tension. The dilatational energy density U_v of a linear elastic material is given by

$$U_v = \frac{3(1-2v)}{2E} \sigma_m^2, \tag{8}$$

where v is Poisson's ratio and E is Young's modulus. Matrix failure is assumed to occur when the dilatational energy density reaches a critical value U_v^{crit} as

$$U_v \geq U_v^{crit} \text{ for } \bar{\sigma} \leq \bar{\sigma}_Y. \tag{9}$$

Here, U_v^{crit} is a constant and was determined to be 0.9 MPa by comparing the cracking strain of the PUC model under uniaxial transverse tension with the failure strain of the experiment for unidirectional 90° laminates.

The second failure criterion is based on damage parameter D, calculated using a ductile damage growth law under plastic deformation. This study uses a damage growth model based on the GTN model,[6–9] which was modified for epoxy resin by

Table 3. Elastic properties of carbon fiber and epoxy resin used in microscopic 3D PUC analysis.

Fiber longitudinal Young's modulus E_L	230 GPa
Fiber transverse Young's modulus E_T	17.5 GPa
Fiber longitudinal Poisson's ratio v_L	0.17
Fiber transverse Poisson's ratio v_T	0.46
Fiber radius r_f	3.5 mm
Fiber's coefficient of thermal expansion for the longitudinal direction a_L	-1.1×10^{-6}/K
Fiber's coefficient of thermal expansion for the transverse direction a_T	10×10^{-6}/K
Matrix Young's modulus E_m	3.2 GPa
Matrix Poisson's ratio v_m	0.38
Matrix's coefficient of thermal expansion a_m	60×10^{-6}/K
ΔT	−100 K

Nishikawa [21]. Damage parameter D, which decreases the stiffness of the matrix resin, is calculated using the following equation.

$$\dot{D} = H(\bar{\sigma} - \bar{\sigma}_Y)(1 - D)C\langle\dot{\varepsilon}_m^p\rangle + (B_0 + B_1 D)\dot{\bar{\varepsilon}}^p \tag{10}$$

$$\text{where } C\langle\dot{\varepsilon}_m^p\rangle = A\left[D\left(\frac{\langle\sigma_m\rangle}{\hat{\sigma}}\right)^2\right]^{\bullet} \tag{11}$$

The first term of the right-hand side in Equation (10) represents void growth caused by the average plastic vertical strain. This term is activated when the von Mises stress exceeds the linear limit, as expressed by the Heaviside function H. The second term indicates the damage evolution caused by plastic deformation. Here, $\hat{\sigma}$ is the reference stress; A, B_0, and B_1 are non-dimensional constants; and $\langle\rangle$ is the Macauley bracket. Matrix failure is assumed to occur when the damage parameter reaches a critical value D^{crit} as

$$D \geq D^{crit} \text{ for } \bar{\sigma} \geq \bar{\sigma}_Y. \tag{12}$$

Here, we performed FEA while applying uniaxial tension and compression to the neat-epoxy model depicted in Figure 3 to determine the constants related to the damage growth law. Each side of the neat-epoxy model was 50 μm long, and the model included an initial void with a diameter of 10 μm at the central position. We then determined that $A = 1.6$, $B_0 = 0.6$, $B_1 = 0.6$, and $\hat{\sigma} = 73$ MPa through comparison with the failure strain in the experiments.[22] The calculated stress–strain curves of neat epoxy using these parameters are plotted in Figure 4. We can see that ductile failure occurs under compression, and that more brittle failure occurs under tension. This tendency is consistent with the experiment results reported in [22], although the magnitude exhibits some differences because the material differs. Therefore, the constants used in this study are reasonable to reproduce the ductile failure behavior of epoxy resin.

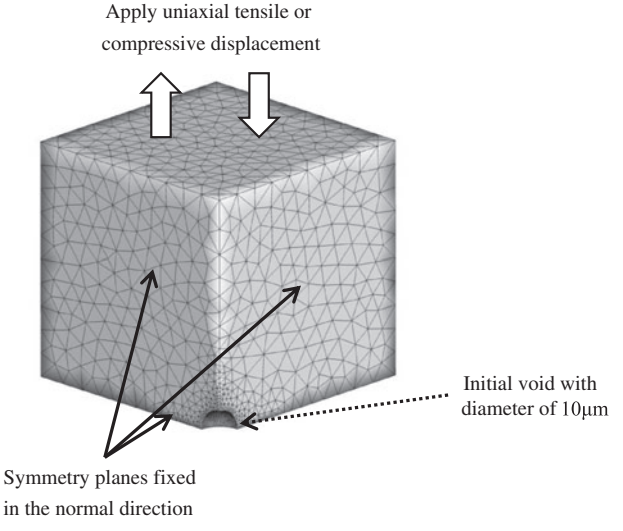

Figure 3. 3D FE model of neat epoxy for determining material constants of the damage growth law.

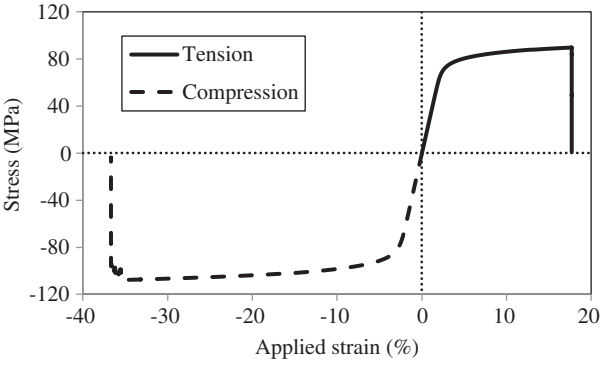

Figure 4. Simulated tensile and compressive stress–strain curves using the neat-epoxy model.

The damage parameter is calculated at integration points based on the damage growth law mentioned above and averaged within each element at each step. To avoid mesh dependence of matrix damage, non-localization of damage parameter D is performed according to Refs [23,24].

$$D(\boldsymbol{x}) = \frac{1}{V_r(\boldsymbol{x})}\int_V h(\boldsymbol{s}-\boldsymbol{x})D_{elem}(\boldsymbol{s})dV(\boldsymbol{s}) \tag{13}$$

Here, D_{elem} is the damage of each element, and V is the reference volume. h and V_r are given by

$$h(\boldsymbol{x}) = \exp\left\{-\frac{k|\boldsymbol{x}|^2}{l^2}\right\}, \tag{14}$$

$$V_r(\boldsymbol{x}) = \int_V h(\boldsymbol{s}-\boldsymbol{x})dV(\boldsymbol{s}). \tag{15}$$

Here, k is the dimensionality ($k=3$ in this study), and l is a reference length for non-localization, with $l=0.15$ μm in this study. Furthermore, $D^*(D)$ is introduced in the following instead of D in Equation (5) to include the effect of sudden damage evolution due to coalescence of micro voids.[24]

$$D^* = \begin{cases} D & (D<D_c) \\ D_c + \frac{D^{*crit}-D_c}{D^{crit}-D_c}(D-D_c) & (D\geq D_c) \end{cases} \tag{16}$$

$$\dot{D}^* = \begin{cases} \dot{D} & (D<D_c) \\ \frac{D^{*crit}-D_c}{D^{crit}-D_c}\dot{D} & (D\geq D_c) \end{cases} \tag{17}$$

Here, D_c is D when starting the coalescence of microvoids, and D^{crit} is D when the element has failed. Equation (10) provides the damage evolution rate, and Equations (16) and (17) yield D^*, which determines the stiffness matrix and stress. At each element under plastic deformation ($\bar{\sigma} > \bar{\sigma}_Y$), we recognize that the element fails when D reaches D^{crit} and remove the stress. This paper uses $D_c = 0.08$, $D^{crit} = 0.25$, and $D^{*crit} = 1/1.5$.

In the PUC analysis, the displacement and strain increments $\Delta \boldsymbol{u}$ and $\Delta \boldsymbol{\varepsilon}$ are separated into global (subscript G) and local (subscript L) components as follows.

$$\Delta \boldsymbol{u} = \Delta \boldsymbol{u}_G + \Delta \boldsymbol{u}_L \tag{18}$$

$$\Delta \boldsymbol{\varepsilon} = \Delta \boldsymbol{\varepsilon}_G + \Delta \boldsymbol{\varepsilon}_L \tag{19}$$

The global components indicate a homogeneous distribution and the local components indicate an inhomogeneous distribution in the unit-cell model. Applying decomposition, the incremental form of the stiffness equation is described as follows [4]

$$({}^t\boldsymbol{K}_f + {}^t\boldsymbol{K}_m)\Delta \boldsymbol{U}_L = -({}^t\boldsymbol{Q}_f + {}^t\boldsymbol{Q}_m) + {}^t\boldsymbol{Q}_v + {}^t\boldsymbol{Q}_{dam} - (\Delta \boldsymbol{Q}_{f,G} + \Delta \boldsymbol{Q}_{m,G}) \tag{20}$$

$$\begin{gathered}
\text{where } \boldsymbol{K}_f = \sum_e \int_{V_f^e} \boldsymbol{B}^{e^T} \boldsymbol{D}_f^e \boldsymbol{B}^e dV, \boldsymbol{K}_m = \sum_e \int_{V_m^e} (1 - D^*) \boldsymbol{B}^{e^T} \boldsymbol{D}_m^e \boldsymbol{B}^e dV, \\
\boldsymbol{Q}_f = \sum_e \int_{V_f^e} \boldsymbol{B}^{e^T} \hat{\boldsymbol{\sigma}} dV, \boldsymbol{Q}_m = \sum_e \int_{V_m^e} \boldsymbol{B}^{e^T} \hat{\boldsymbol{\sigma}} dV, \\
\boldsymbol{Q}_v = \sum_e \int_{V_m^e} (1 - D^*) \frac{3\mu \Delta \bar{\varepsilon}^p}{\bar{\sigma}} \boldsymbol{B}^{e^T} \hat{\boldsymbol{\sigma}}' dV, \\
\boldsymbol{Q}_{dam} = \sum_e \int_{V_m^e} \frac{\Delta D^*}{1 - D^*} \boldsymbol{B}^{e^T} \hat{\boldsymbol{\sigma}} dV, \\
\Delta \boldsymbol{Q}_{f,G} = \sum_e \int_{V_f^e} \boldsymbol{B}^{e^T} \boldsymbol{D}_f^e \Delta \boldsymbol{\varepsilon}_G dV, \\
\Delta \boldsymbol{Q}_{m,G} = \sum_e \int_{V_m^e} \boldsymbol{B}^{e^T} \boldsymbol{D}_m^e \Delta \boldsymbol{\varepsilon}_G dV.
\end{gathered} \tag{21}$$

Here, subscripts f and m represent the fiber and matrix regions. $\boldsymbol{U}$ is the nodal displacement vector, $\boldsymbol{K}$ is the stiffness matrix of fiber and matrix, $\boldsymbol{Q}$ is the internal force vector, $\boldsymbol{B}$ is the compatibility matrix of strain and displacement, and $\boldsymbol{D}$ is the matrix form of the constitutive law. The formulation of the incremental stiffness equation can be seen in Ref [4]. The simulation is controlled by the global strain increment, which is determined based on the strain history obtained from the macroscopic 3D FEA.

2.3. *Computational procedure of multiscale modeling*

The strain history at a point in laminates, obtained from macroscopic 3D FEA, is used as the global strain increment in the PUC simulation. Therefore, a position of crack initiation in specimens needs to be determined first. Here, it is well known that strong in-plane shear deformation appears near the end tabs, and this may cause crack initiation. However, it is difficult to model a boundary condition which represents a realistic constraint of end tabs in macroscopic 3D FEA, since relaxation of constraints will occur by plastic deformation and peeling of adhesive layers in the end tabs. In addition, experiments exhibited failure at the center in longitudinal direction in some specimens, although many specimens failed near the end tabs. For these reasons, crack is assumed to occur at the center in the longitudinal direction as seen in Figure 5, to avoid effects

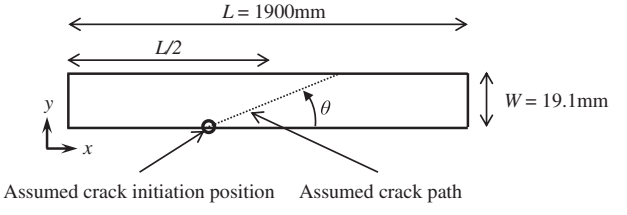

Figure 5. Assumed position of crack initiation and crack path in coupon specimens.

of the uncertainties of the constraint on crack prediction. In addition, we use a FE model with 10-times length of actual specimens to eliminate the effect of end tabs completely.

The computational procedure of the multiscale modeling is summarized as follows:

Step 1. Perform macroscopic 3D FEA applying incremental uniaxial external displacement to the coupon model for each off-axis angle. During the analysis, the strain history at the point indicated in Figure 5 is extracted and stored.

Step 2. Calculate the unit-cell model, decreasing from the curing temperature to room temperature. Here, we adjust the incremental global strain by a simple feedback approach so that the global stress components are zero (i.e. $\boldsymbol{\sigma}_G = 0$). The stress/strain field obtained from this calculation is assumed as the initial state.

Step 3. Apply the strain history obtained in *Step 1* to the global strain increments of the microscopic 3D PUC model. The initial cracking strain is defined as applied strain to the laminates when the first matrix element is judged as fractured based on Equation (9) or Equation (12).

We also perform a PUC analysis under transverse uniaxial tension for 90° axis specimens to compare the simulated results with experiment, and to discuss the failure mechanisms in microscopic structure.

3. Experiments

We performed uniaxial tensile tests on unidirectional off-axis laminates to obtain the nonlinear stress–strain curves and failure strains. The unidirectional laminates used in this study consisted of carbon fiber and epoxy resin (Toray, T700G/2511). The measured fiber volume fraction was 56%. The angles of fiber directions in laminates tested in this study were 15°, 20°, 30°, 45°, 60°, 75°, and 90°. The dimensions of the specimens are presented in Figure 6. Rectangular end tabs made of GFRP were glued on using a room temperature setting adhesive, Araldite^{TM}. The end tabs were 1 mm thick. Uniaxial tensile loading was applied to these specimens using a general mechanical testing machine (MTS810) at a displacement rate of 0.01 mm/s.

Here, we need to determine the relationship between the effective stress $\bar{\sigma}$ and effective plastic strain $\bar{\varepsilon}^p$ presented by Equations (3) and (4), based on the experiment results for off-axis specimens. The effective stress $\bar{\sigma}$ and the effective plastic strain $\bar{\varepsilon}^p$ are described by the tensile stress σ_x and plastic strain in tensile direction ε_x^p as follows [13]:

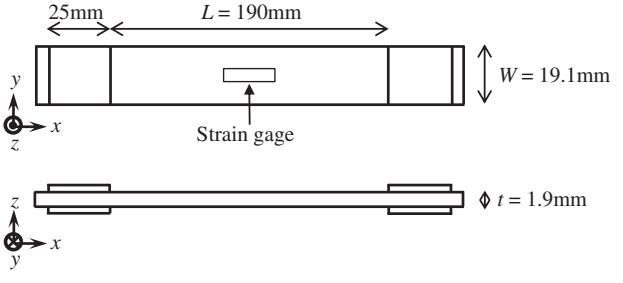

Figure 6. Dimensions of coupon specimens for uniaxial off-axis tensile tests.

$$\bar{\sigma} = (h(\theta) + a_1)\sigma_x \tag{22}$$

$$\bar{\varepsilon}^p = \frac{\varepsilon_x^p}{h(\theta) + a_1} \tag{23}$$

$$\begin{aligned} \text{where } h(\theta) &= \sqrt{\tfrac{3}{2}\sin^4\theta + 3a_{66}\sin^2\theta\cos^2\theta + a_1^2\cos^4\theta} \quad (\sigma_x \geq 0) \\ h(\theta) &= -\sqrt{\tfrac{3}{2}\sin^4\theta + 3a_{66}\sin^2\theta\cos^2\theta + a_1^2\cos^4\theta} \quad (\sigma_x \leq 0) \end{aligned} \tag{24}$$

Here, θ is the off-axis angle of the specimens. ε_x^p can be obtained from the following equation.

$$\varepsilon_x^p = \varepsilon_x - \frac{\sigma_x}{E_x} \tag{25}$$

Using Equations (22)–(25), the tensile stress–strain curves can be converted to effective stress-effective plastic strain curves. The converted curves for each off-axis specimen depend on parameters a_{66} and a_1. We fixed $a_1 = 0.01$ referring to [13] and determined $a_{66} = 1.6$ by collapsing the results of different off-axis specimens into one master curve. We can then determine the constants in the power law in Equations (3) and (4) such that the power laws reproduce the master curve. The parameters listed in Table 1 were determined in this way.

4. Results and discussion

Figure 7 provides the effective stress-effective plastic strain curves calculated from the tensile stress–strain relations observed in the experiment for each specimen. Curves calculated from Equations (3) and (4) are also presented. As seen in Figure 7, the curves of the effective stress-effective plastic strain for all off-axis laminates collapsed well into one master curve when the constants listed in Table 1 were used, and we can see that the approximation using Equations (3) and (4) successfully reproduces the master curve. Figure 8 compares the tensile stress–strain curves simulated by the macroscopic 3D FEA mentioned in Section 2.1 with those obtained from the experiments. For all off-axis angles, the simulated results are consistent with the experiments.

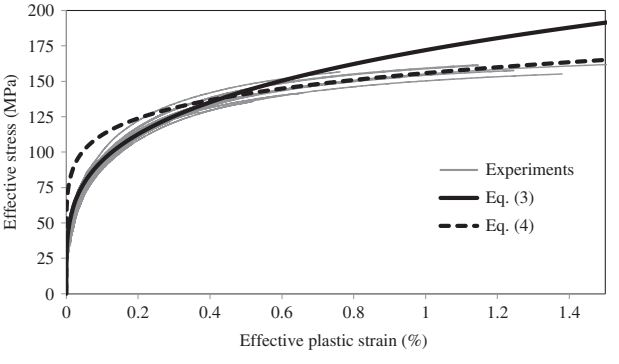

Figure 7. Effective stress-effective plastic strain curves converted from the tensile stress–strain relationship in the experiments, and curves approximated using Equations (3) and (4).

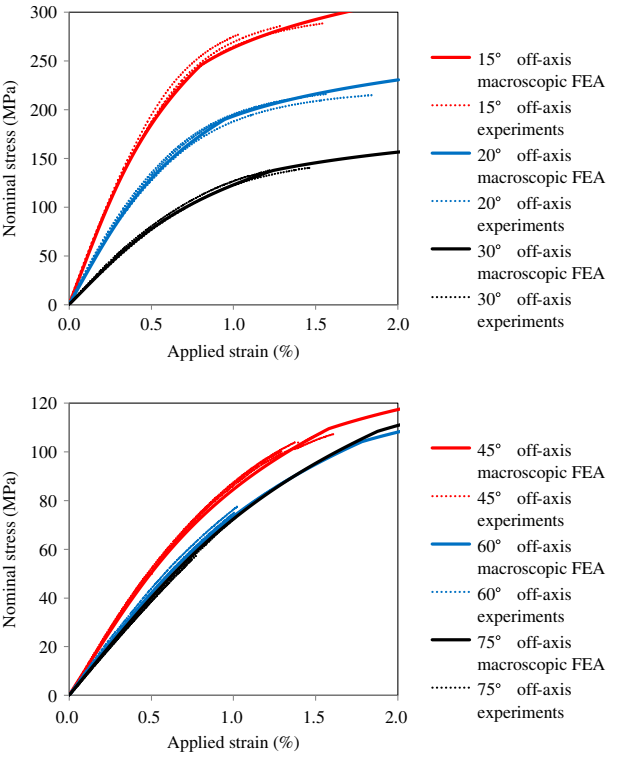

Figure 8. Comparison of tensile stress–strain curves for each off-axis laminate between the macroscopic FEA and the experiments.

Figure 9 compares the stress–strain curves obtained from the PUC analysis under transverse uniaxial tension with those of the experiments on 90° specimens. Here, it should be noted that we cannot compare the stress–strain curves of other off-axis laminates simulated by PUC analyses with those obtained from experiments because the off-axis specimens exhibit inhomogeneous deformation in the coupon specimens. We can see in Figure 9 that the stiffness and failure strain determined by PUC analysis are consistent with those of the experiments. The cracking patterns under transverse uniaxial tension illustrated in Figure 10(a)–(c) correspond to those indicated in Figure 9. In Figure 10, the green elements indicate matrix elements that failed due to the dilatational energy density criterion (Equation (9)), and the red elements indicate that failed due to ductile damage growth (Equation (12)). At first, the crack initiates by dilatation near the pole of fibers arranged parallel to the loading direction. The crack then propagates due to the ductile damage growth. This failure mechanism is consistent with the explanation presented by Asp et al. [11,12], and thus we can consider that the combination of the two failure criteria employed in this study reasonably reproduce the mechanism of crack initiation under transverse uniaxial tension.

The cracking patterns of 30° and 60° off-axis laminates are depicted in Figure 11. As seen in this figure, the matrix cracks occur due to ductile damage growth (red elements in figures), although the position of crack initiation is the same as that occurring under uniaxial transverse tension. This tendency appears in all off-axis laminates except

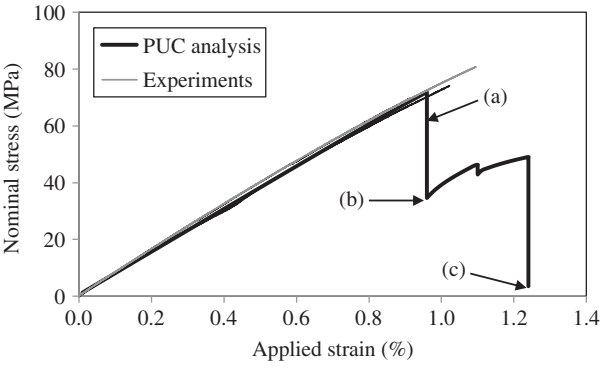

Figure 9. Comparison of tensile stress–strain curve for 90° axis laminate between the microscopic PUC analyses and the experiments.

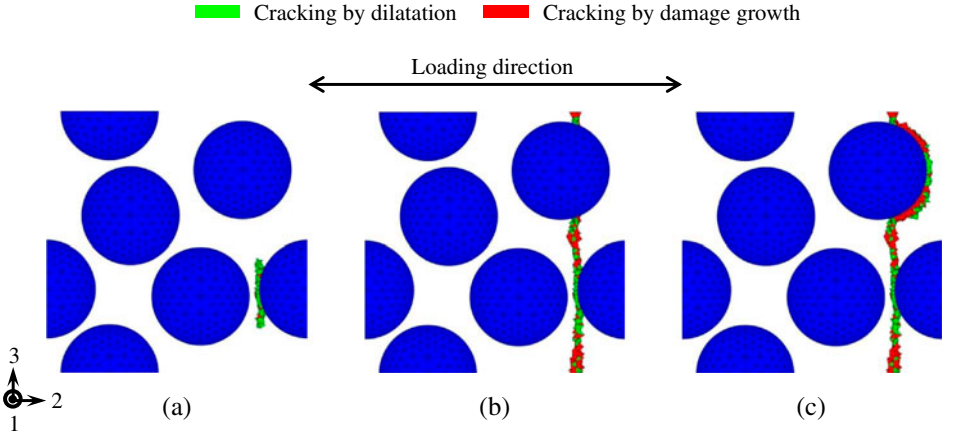

Figure 10. Cracking pattern in the PUC model under transverse uniaxial tension.

75° and 90°. The plastic strain due to shear deformation between two fibers is the main cause of crack initiation for off-axis laminates in which the angle of the fiber direction is smaller than 60°. In these off-axis laminates, the dilatational energy density criterion is not appropriate for predicting crack initiation in the matrix.

The von Mises stress distributions for unidirectional 30°, 60°, and 90° laminates just before the crack initiation are presented in Figure 12. The von Mises stress at the cracking position in 90° laminate is quite small and plastic deformation does not occur at all, as reported by Asp et al. [11,12]. In contrast, the von Mises stress at the cracking position in 30° and 60° off-axis laminates becomes higher, resulting in yielding of matrix at that region. This high von Mises stress is derived from the shear deformation in matrix between two fibers, as a result of macroscopic in-plane shear deformation. Therefore, matrix failure in off-axis laminates is dominated by ductile damage growth under plastic deformation.

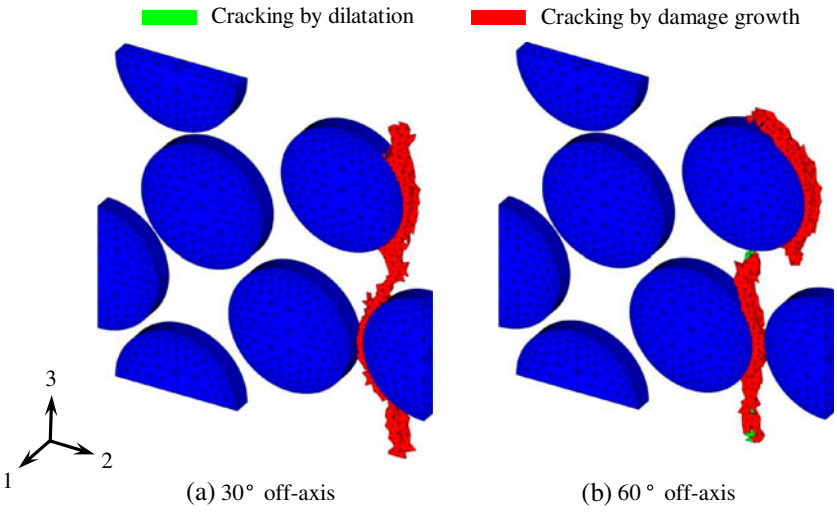

Figure 11. Cracking patterns in the PUC model for 30° and 60° off-axis laminates.

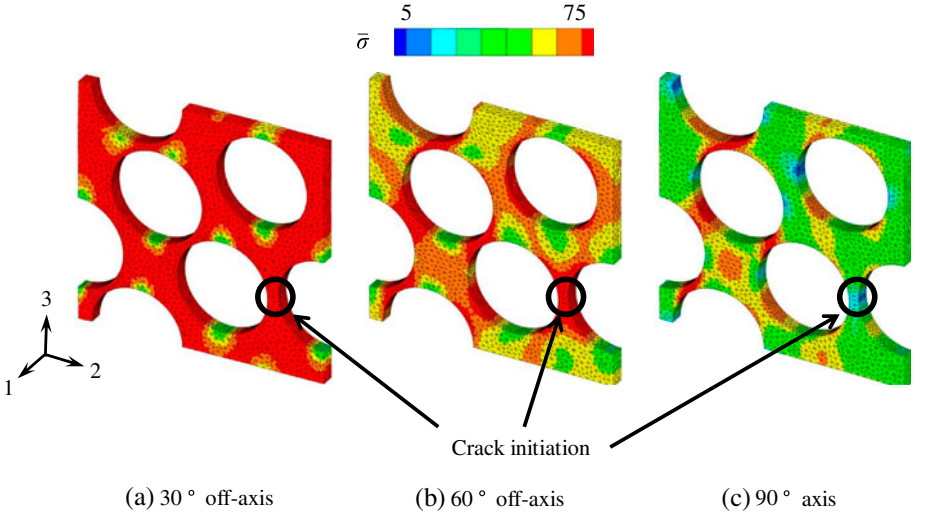

Figure 12. Distribution of the von Mises stress in the PUC model for 30°, 60°, and 90° laminates.

Figure 13 compares the crack initiation strains obtained by the multiscale analyses with the failure strains in the experiments. The crack initiation strains of the off-axis laminates are consistent with the failure strains in the experiments. This validates the accuracy of the multiscale modeling in this study.

In this study, crack initiation was assumed to occur at the center in the longitudinal direction, and effects of the constraints of the end tabs were not considered. However, a boundary condition which represents a realistic constraint should be modeled in order to explain the failure position in experiments, and this will be our future work.

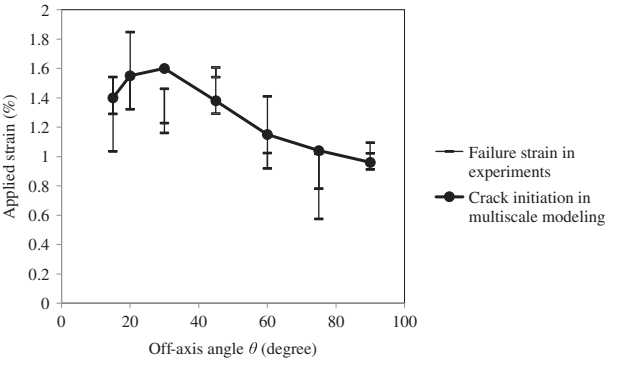

Figure 13. Comparison of the simulated crack initiation strains with the failure strains in the experiment.

5. Conclusions

We numerically predicted crack initiation in unidirectional off-axis laminates using a multiscale approach. In addition, we performed a series of uniaxial tensile tests on unidirectional off-axis laminates with several fiber angles to obtain and compare their nonlinear stress–strain relationship and failure properties. These multiscale analyses demonstrated that the failure criteria employed in this study are reasonable for reproducing the failure mechanism under transverse tension as reported by Asp et al. [11,12]; that is, dilatation-induced brittle failure occurs first, followed by failure governed by ductile damage growth. However, the crack initiation was caused by ductile damage growth, not by dilatation under elastic deformation, in off-axis laminates with small angles ($\theta \leq 60°$). The applied strains when the initial crack occurs were consistent with the failure strains in the experiments. Therefore, we must consider a damage growth under plastic deformation for predicting crack initiation in composites under a general combined loading.

Acknowledgments

T.O. thanks Toray Industries, Inc. and Toray Composites (America), Inc. for support of this study.

References

[1] Camanho PP, Davila CG, de Moura MF. Numerical simulation of mixed-mode progressive delamination in composite materials. J. Compos. Mater. 2003;37:1415–1438.
[2] Hallett SR, Jiang WG, Khan B, Wisnom MR. Modelling the interaction between matrix cracks and delamination damage in scaled quasi-isotropic specimens. Compos. Sci. Technol. 2008;68:80–89.
[3] Canal LP, Segurado J, LLorca J. Failure surface of epoxy-modified fiber-reinforced composites under transverse tension and out-of-plane shear. Int. J. Solids Struct. 2009;46:2265–2274.
[4] Okabe T, Nishikawa M, Toyoshima H. A periodic unit-cell simulation of fiber arrangement dependence on the transverse tensile failure in unidirectional carbon fiber reinforced composites. Int. J. Solids Struct. 2011;48:2948–2959.
[5] Jeong HY. A new yield function and a hydrostatic stress-controlled void nucleation model for porous solids with pressure-sensitive matrices. Int. J. Solids Struct. 2002;39:1385–1403.

[6] Gurson AL. Continuum theory of ductile rupture by void nucleation and growth: part I – yield criteria and flow rules for porous ductile media. J. Eng. Mater. Technol. 1977;99:2–14.
[7] Needleman A, Tvergaard V. An analysis of ductile rupture in notched bars. J. Mech. Phys. Solids 1984;32:461–490.
[8] Tvergaard V. On localization in ductile materials containing spherical voids. Int. J. Fract. 1982;18:237–252.
[9] Tvergaard V, Needleman A. Analysis of the cup-cone fracture in a round tensile bar. Acta Metall. 1984;32:157–169.
[10] Hobbiebrunken T, Hojo M, Adachi T, Jong CD, Fiedler B. Evaluation of interfacial strength in CF/epoxies using FEM and *in situ* experiments. Composites Part A. 2006;37:2248–2256.
[11] Asp LE, Berglund LA, Talreja R. Prediction of matrix-initiated transverse failure in polymer composites. Compos. Sci. Technol. 1996;56:1089–1097.
[12] Asp LE, Berglund LA, Talreja R. A criterion for crack initiation in glassy polymers subjected to a composite-like stress state. Compos. Sci. Technol. 1996;56:1291–1301.
[13] Yokozeki T, Ogihara S, Yoshida S, Ogasawara T. Simple constitutive model for nonlinear response of fiber-reinforced composites with loading-directional dependence. Compos. Sci. Technol. 2007;67:111–118.
[14] Sun CT, Chen JL. A simple flow rule for characterizing nonlinear behavior of fiber composites. J. Compos. Mater. 1989;23:1009–1020.
[15] Weeks CA, Sun CT. Modeling non-linear rate-dependent behavior in fiber-reinforced composites. Compos. Sci. Technol. 1998;58:603–611.
[16] Kobayashi S, Tomii D, Shizawa K. A modelling and simulation on failure prediction of ductile polymer based on craze evolution and annihilation. Trans. Jpn. Soc. Eng. 2004;70:810–817. (in Japanese).
[17] de Souza Neto EA, Peri D, Owen DRJ. Computational methods for plasticity. New York (NY): Wiley; 2008.
[18] Lemaitre J. How to use damage mechanics. Nucl. Eng. Des. 1984;80:233–245.
[19] Murakami S. Continuum damage mechanics: a continuum mechanics approach to the analysis of damage and fracture. New York (NY): Springer; 2012.
[20] Matsuda T, Ohno N, Tanaka H. Homogenized in-plane elastic-viscoplastic behavior of long fiber-reinforced laminates. JSME Int. J. Ser. A. 2002;45:538–544.
[21] Nishikawa M. Multiscale modeling for the microscopic damage and fracture of fiber-reinforced plastic composites [Dr Eng. Thesis]. Tokyo: The University of Tokyo; 2008. (in Japanese).
[22] Fiedler B, Hojo M, Ochiai S, Schulte K, Ando M. Failure behavior of an epoxy matrix under different kinds of static loading. Compos. Sci. Technol. 2001;61:1615–1624.
[23] Pijaudier-Cabot G, Bažant ZP. Nonlocal damage theory. J. Eng. Mech. 1987;113:1512–1533.
[24] Tvergaard V, Needleman A. Effects of nonlocal damage in porous plastic solids. Int. J. Solids Struct. 1995;32:1063–1077.